








Cite this: *J. Mater. Chem. C*, 2021,  
9, 3901

## Inverted organic photovoltaics with a solution-processed ZnO/MgO electron transport bilayer†

Ioannis Ierides, <sup>a</sup> Isaac Squires, <sup>a</sup> Giulia Lucarelli, <sup>b</sup> Thomas M. Brown <sup>b</sup>  
and Franco Cacialli <sup>\*a</sup>

Electron transport layers (ETLs) have been instrumental in breaking the efficiency boundaries of solution-processed photovoltaics. In particular, bilayer ETLs with an MgO top component have afforded tremendous success in various solution-processed systems, such as perovskite photovoltaics, however, their application in the promising technology of organic photovoltaics is limited. In this work, we fabricate organic photovoltaic devices incorporating a “bilayer” ZnO/MgO ETL instead of a single ZnO ETL, so as to reduce the leakage current and boost the power conversion efficiency. The ZnO/MgO ETL is shown to have a more uniform top surface and a lower work function compared to the single ZnO ETL which is expected to be beneficial to electron extraction. Furthermore, we demonstrate that insertion of the thin ( $\lesssim 10$  nm) MgO interlayer in devices leads to a reduced leakage current and an increase in the shunt resistance. Application of the MgO interlayer boosts the short circuit current density and fill factor, and enhances the power conversion efficiency by  $\sim 10\%$  (relative increase) thereby demonstrating a facile approach to push the efficiency of organic photovoltaics to higher levels.

Received 19th October 2020,  
Accepted 15th February 2021

DOI: 10.1039/d0tc04955g

rsc.li/materials-c

## 1 Introduction

Solution-processed photovoltaic systems benefit from the advantage of cheap fabrication over large areas and provide windows of opportunity for novel photovoltaic applications.<sup>1,2</sup> Hence intense research efforts have been focused on both organic and inorganic solution-processed systems, ranging from quantum dots,<sup>3</sup> polymers<sup>4,5</sup> and small molecules<sup>6</sup> to perovskite photovoltaics.<sup>7–9</sup>

A common strategy employed to increase efficiency in the vast majority of these systems is the implementation of a multilayer stack, where the active layer is sandwiched between an electron transport layer (ETL) and a hole transport layer (HTL) prior to the addition of electrodes on either side. These layers can serve different functions in each of the aforementioned systems. They can be used to modify the interfacial energetics of the device<sup>10</sup> by matching and controlling the work function of different components and thus increase the built-in field,<sup>11</sup> and/or form ohmic contacts,<sup>12</sup> to name but a few

examples. Ultimately, their common purpose in all cases is to facilitate charge transport and extraction.

In the case of inverted organic photovoltaics (OPVs), a plethora of materials have been investigated for application as ETLs. For a comprehensive review we direct the reader to the review by Yin *et al.*<sup>12</sup> A key example is the polymer poly[(9,9-bis(3'-(*N,N*-dimethylamino)propyl)-2,7-fluorene)-*alt*-2,7-(9,9-dioctyl-fluorene)] known as PFN<sup>13</sup> that is used to reduce the work function of ITO. There are of course many other examples.<sup>14,15</sup> Interestingly, the prevailing ETLs in inverted OPVs are semiconducting metal oxides since they have the combined ability to effectively extract/transport electrons due to their relatively high mobilities and at the same time offer good solution-processability, high optical transparency and good environmental stability.<sup>12</sup> The most widely employed metal oxide is ZnO. Indeed, ZnO has been the “elective” ETL for the latest state-of-the-art inverted OPV devices<sup>16,17</sup> affording higher efficiency than other metal oxides such as TiO<sub>2</sub>.

However, solution-processed ZnO is a sub-optimal ETL. For example, it can suffer from surface defects that can act as electron trap sites and result in severe charge recombination losses.<sup>18,19</sup> The application of a thin or ultrathin interlayer between ZnO and the active layer to form a bilayer ETL has proven to be a simple and effective method to improve ZnO-based inverted OPVs through various mechanisms (incidentally, some of these interlayers, also because of their

<sup>a</sup> Department of Physics and Astronomy and London Centre for Nanotechnology, University College London, London, WC1H 0AH, UK. E-mail: f.cacialli@ucl.ac.uk; Tel: +44 (0)20 7679 4467

<sup>b</sup> CHOSE (Centre for Hybrid and Organic Solar Energy), Department of Electronic Engineering, University of Rome Tor Vergata, Italy

† Electronic supplementary information (ESI) available. See DOI: 10.1039/d0tc04955g

reduced thickness, lack morphological uniformity, to the point of calling into question the appropriateness of the “bilayer” diction – for convenience, and following the practice of previous literature, we will still refer in some places to the combined ZnO/MgO ETL as a “bilayer” even though some evidence is presented that our MgO films also lack uniformity, so that a more accurate description might be that of an “interlayer” for the ZnO/MgO combination).

For example, Abd-Ellah *et al.*<sup>20</sup> employed a carboxylic acid as the modifying interlayer that decreased the work function of the ETL by  $\sim 0.4$  eV, and boosted both the short-circuit current density ( $J_{sc}$ ) and fill factor (FF) with respect to devices based on a single ZnO ETL. Similarly, Wang *et al.*<sup>18</sup> formed a ZnO/In ETL nanojunction with indium films ( $\leq 1$  nm thick) that reduced recombination by filling the traps, and decreased the contact barrier potential thereby facilitating carrier transport and extraction. In addition, formation of  $\text{In}_2\text{O}_3$  provided an efficient energy cascade from the fullerene component of the active layer to ZnO. An increase in  $J_{sc}$  and the FF has also been achieved by the passivation of traps on the surface of ZnO through the formation of bilayer ETLs with  $\text{MoS}_2$  quantum dots,<sup>19</sup> poly(vinylpyrrolidone) and polyethylene glycol,<sup>21</sup> calcium fluoride<sup>22</sup> and solid alcohol 1-pyrenemethanol<sup>23</sup> serving as the modifying interlayers. Other interlayers such as a pyrene BODIPY molecular dye<sup>24</sup> and commercially available dispersants D181 and D187<sup>25</sup> applied between ZnO and the active layer, optimised the active layer morphology. Recently, it has been demonstrated that biomaterials such as DNA<sup>26</sup> and processed spinach leaves<sup>27</sup> can serve as effective modifying interlayers in bilayer ZnO ETLs. In all the above cases the use of a bilayer ETL led to enhanced power conversion efficiencies (PCEs) when compared with a single ZnO ETL. The recent resurgence of OPVs<sup>2</sup> has led to device efficiencies exceeding 18%<sup>28</sup> in state-of-the-art single junctions. The application of a bilayer ETL rather than a single ETL may enable further efficiency improvements. This motivated us to search for other materials that can be applied successfully as modifying interlayers.

Recent studies of other solution-processed photovoltaic systems with a bilayer ETL based on MgO captured our attention. Dagar and collaborators<sup>29</sup> for example demonstrated  $\text{SnO}_2/\text{MgO}$  bilayer ETLs in  $\text{CH}_3\text{NH}_3\text{PbI}_3$  perovskite cells reaching efficiencies up to 19% under 1 sun. This represented an increase of  $\sim 20\%$  compared to the single  $\text{SnO}_2$  ETL that was attributed to an improved ETL film quality as the presence of MgO removed pinholes on the  $\text{SnO}_2$  surface, and to a reduced interfacial carrier recombination. Similarly, Han *et al.*<sup>30</sup> employed a  $\text{TiO}_2/\text{MgO}$  bilayer ETL improving the efficiency by  $\sim 10\%$  compared to the single  $\text{TiO}_2$  ETL. Besides  $\text{CH}_3\text{NH}_3\text{PbI}_3$  perovskites the use of a bilayer ETL incorporating MgO as a top component (and thus in contact with the active layer) has also been demonstrated in other solution-processed systems. Jayaweera *et al.*<sup>31</sup> used an  $\text{SnO}_2/\text{MgO}$  ETL effectively to form CdS nanosheet sensitized photovoltaics. This study was preceded by the study of Docampo *et al.*,<sup>32</sup> where an  $\text{SnO}_2/\text{MgO}$  bilayer ETL was applied to both solid state and electrolyte dye sensitised solar cells leading to a tripling and almost doubling of the efficiency for the two cases respectively,

compared to their single  $\text{SnO}_2$  ETL counterparts. By employing transient photovoltage and charge collection measurements it was demonstrated that the presence of MgO favorably shifts the conduction band edge of the ETL by 200 mV, thereby partly enabling the increase in open circuit voltage ( $V_{oc}$ ), hence increasing performance. It is important to note that the mechanism by which the bilayer MgO based ETL facilitated the performance enhancement with respect to having a single ETL, differs in each of the above instances and necessitates a separate investigation in each case to uncover it. MgO has a very high ionisation potential ( $\sim 10$  eV – see Fig. 1a) and an insulating nature. These characteristics may serve to decrease the current leakage in OPV devices. The question therefore arises as to whether MgO could be applied effectively as a modifying interlayer in OPVs so as to increase their performance.

In this work, we investigate MgO as a modifying interlayer on top of a ZnO ETL formed by simple solution-processing and low temperature annealing and apply it to OPVs (see Fig. 1b for the OPV device structure). We show that the modified ETL enhances the performance of OPV devices with respect to the single ZnO ETL. The use of an MgO interlayer for OPVs has not been reported previously, with the exception of a very recent publication<sup>33</sup> that uses a different device architecture (namely with the MgO not in direct contact with the active layer but “buried” below the ZnO film), and of which we became aware of in the final stages of the preparation of this manuscript. Both studies show that the application of MgO in ETLs for OPVs can lead to enhanced performance, thus demonstrating the excellent potential of MgO. In the study by Huang *et al.*<sup>33</sup>  $\text{FTO}/\text{MgO}/\text{ZnO}$  is used for electron extraction. In our study, the electron extractor system is  $\text{ITO}/\text{ZnO}/\text{MgO}$  and MgO is used as the top component of the system. To investigate the origin of the performance enhancement resulting from the addition of MgO in our device structure, in addition to the typical current density–voltage and external quantum efficiency (EQE) characterisation of our devices, we present atomic force microscopy (AFM), Kelvin probe measurements and optical spectroscopy (namely transmittance, absorbance and electroabsorption). These measurements enable us to demonstrate that insertion of the thin ( $\leq 10$  nm) MgO interlayer in OPV devices leads to reduced leakage current and an increase in the shunt resistance by a factor of 2 compared to devices with only a single ZnO ETL. Furthermore, we show that the ZnO/MgO ETL has a more uniform top surface with a root mean square (rms) roughness decreasing from  $4.5 \pm 0.2$  nm to  $3.2 \pm 0.4$  nm and a lower work function by  $0.11 \pm 0.05$  eV. We discuss the origin of the (slightly) lower work function that seems to be associated with the electrostatic compression effect of  $\text{MgO}$ <sup>34</sup> on metal oxides.

## 2 Experimental

### 2.1 Device fabrication

**2.1.1 Materials.** For the investigations, we have used the following widely available commercial materials: poly[4,8-bis(5-(2-ethylhexyl)thiophen-2-yl)benzo[1,2-*b*;4,5-*b'*]dithiophene-2,6-



diyl-*alt*-(4-(2-ethylhexyl)-3-fluorothieno[3,4-*b*]thiophene)-2-carboxylate-2,6-diyl)] (PTB7-Th), [6,6]-phenyl-C71-butyric acid methyl ester (PC<sub>70</sub>BM), 3,9-bis(2-methylene-((3-(1,1-dicyanomethylene)-6,7-difluoro)-indanone))-5,5,11,11-tetrakis(4-hexylphenyl)-dithieno [2,3-*d*:2',3'-*d'*]-*s*-indaceno[1,2-*b*:5,6-*b'*]dithiophene (ITIC-2F) and poly(9,9-dioctylfluorene-*alt*-benzothiadiazole) (F8BT). The above materials were purchased from Ossila and their chemical structures can be found in Fig. S1 (ESI†). Zinc acetate dihydrate, 2-methoxyethanol, ethanolamine, magnesium acetate tetrahydrate, tin chloride dihydrate, ethanol, acetone, isopropanol and toluene were purchased from Sigma Aldrich. Chlorobenzene was purchased from Acros organics and 1,8-diiodooctane was purchased from Alfa Aesar. Evaporation materials Au, Ag and MoO<sub>3</sub> were purchased from Kurt J. Lesker. Glass/ITO substrates were purchased from Ossila.

**2.1.2 Preparation of solutions.** The PTB7-Th:PC<sub>70</sub>BM blend solution was formed by initially dissolving 15 mg of PTB7-Th in 1.5 mL chlorobenzene mixed with 45  $\mu$ L of 1,8-diiodooctane. The solution was stirred at 70 °C for 4 hours. Then 22.5 mg of PC<sub>70</sub>BM were added to yield a 25 mg mL<sup>-1</sup> concentration with blend ratio of 1:1.5. The solution was then allowed to stir overnight at room temperature. All the above processes were carried out in a glovebox under a nitrogen environment. The PTB7-Th:ITIC-2F solution was formed by dissolving 10 mg of PTB7-Th in 1 mL chlorobenzene and 15 mg of ITIC-2F in 0.25 mL of chlorobenzene. The individual solutions were stirred for 4 hours and then mixed together along with 26  $\mu$ L of 1,8-diiodooctane to yield a 20 mg mL<sup>-1</sup> concentration with blend ratio of 1:1.5. The solution was then allowed to stir overnight at room temperature. The above processes were carried out in a glovebox under a nitrogen environment as well. The F8BT solution was formed by dissolving 10 mg of F8BT in 1 mL of toluene. The solution was then allowed to stir overnight at room temperature in the nitrogen glovebox. The ZnO solution was formed by dissolving 0.1 g zinc acetate dihydrate and 28  $\mu$ L ethanolamine in 1 mL of 2-methoxyethanol. The solution was then stirred vigorously for 12 hours at room temperature. The SnO<sub>2</sub> solution was formed by dissolving 45.13 mg of tin chloride dihydrate in 2 mL ethanol and stirring overnight at room temperature. The MgO solution was formed by dissolving 5 mg of magnesium acetate tetrahydrate in 1 mL of ethanol and stirring overnight at room temperature.

**2.1.3 Device fabrication.** The first step to form the ITO/ZnO/MgO/PTB7-Th:PC<sub>70</sub>BM/MoO<sub>3</sub>/Au OPV structure (shown in Fig. 1b) is the cleaning of glass/ITO substrates (Ossila ITO glass substrates – pixelated anode (S101)) in an ultra-sonicator sequentially, using soapy water, acetone and isopropanol for 10 minutes in each case. The substrates were then dried with a nitrogen spray gun. A ~30 nm (as measured by a profilometer) ZnO layer was then formed by spin-coating the ZnO solution on top of the substrate at 3000 revolutions per minute (rpm) for 30 seconds, followed by 1 hour annealing at 150 °C in air. The ~10 nm MgO layer was then formed by spin-coating the MgO solution on top of the ZnO layer at 5000 rpm for 30 seconds, followed by 1 hour annealing at 150 °C in air. Devices with a thicker ~150 nm MgO layer were formed by spin-coating the

MgO solution at 3000 rpm for 30 seconds, followed by 1 hour annealing at 150 °C in air. Samples were then transferred to a nitrogen glovebox for the deposition of the PTB7-Th:PC<sub>70</sub>BM active layer. This was deposited *via* spin-coating at 670 rpm for 60 seconds. The samples were then masked and loaded into a metal evaporator (also housed in the nitrogen glove-box) that was evacuated to a residual pressure of  $1.6 \times 10^{-6}$  mbar before evaporation. A 10 nm MoO<sub>3</sub> layer was then thermally evaporated with a rate of 0.1 Ångstrom second<sup>-1</sup> (Å s<sup>-1</sup>). This was followed by thermal evaporation of 80 nm of Au at rate of 0.2 Å s<sup>-1</sup>. These devices were completed by encapsulation with an epoxy resin (Ossila E132), and glass cover slips (Ossila C181), and by application of electrical connection legs (Ossila E241). In our studies, a range of other structures have been employed to form OPVs. The same fabrication processes has been followed for these devices as well, with minor modifications. Specifically, if no MgO is found in the structure, the process is identical but skipping the MgO deposition and its 1 hour annealing step. Similarly, when no HTL is applied in the structure, the evaporation of MoO<sub>3</sub> is skipped. In the case where Ag is used as a top contact rather than Au, this is evaporated under  $1.6 \times 10^{-6}$  mbar pressure at 0.25 Å s<sup>-1</sup> to form a 100 nm contact. In the case where PTB7-Th:ITIC-2F instead of PTB7-Th:PC<sub>70</sub>BM was used as the active material, this was spin-coated inside the glovebox at 1000 rpm for 90 seconds. Lastly, for devices employing the SnO<sub>2</sub> ETL, this was formed *via* a two-step spin-coating process first at the spin speed of 1500 rpm for 30 seconds, followed by a further 30 seconds at 2500 rpm, to form a ~24 nm thick layer. The layer was then annealed for 1 hour at 150 °C in air.

For the transmittance/absorbance, AFM and Kelvin probe investigations we prepared samples with varying structures. All layers in these samples were processed with the same conditions used for the corresponding layers in OPVs.

Lastly, samples intended for the testing of the ITO and ITO/SnO<sub>2</sub> substrates *via* electroabsorption spectroscopy were fabricated in the same manner as OPVs, but instead of a blend, F8BT was employed as the active layer that was deposited *via* spin-coating at 1000 rpm for 90 seconds in the nitrogen glovebox. These samples were not encapsulated and their measurement was carried out under vacuum ( $\sim 10^{-3}$  mbar).

## 2.2 Device characterisation

**2.2.1 Current density–voltage & external quantum efficiency measurements.** Current density–voltage characteristics under illumination and in darkness, were obtained using a source-measure-unit (SMU) Keithley 2400 and a class AAA solar simulator (ABET Technologies, model Sun 3000 11016A). For measurements under illumination, the output of the lamp was calibrated to 1 sun using a standard Si photodetector. The  $J_{sc}$ ,  $V_{oc}$ , FF and PCE were extracted from the current density *vs.* voltage ( $J$ - $V$ ) characteristics. Dark curves were analysed further to extract the shunt resistance as detailed in Section S2 and Fig. S7 (ESI†). EQE spectra were obtained using a home-built system that uses a monochromated xenon lamp. The power density is extracted *via* the use of a calibrated Bentham DH-Si



photodiode connected to an amplifier, while the current density output from the tested device is recorded simultaneously. To perform the measurements a Keithley 2400 SMU is employed. To extract the calculated short circuit current density of devices the typical 1 sun spectrum was used. The results reported are averages from at least 7 devices in each investigation. Masking of contacts was used as appropriate.

**2.2.2 Absorbance, transmittance, profilometry & atomic force microscopy measurements.** Absorbance and transmittance measurements were carried out by using an Agilent 8453 UV-vis spectrophotometer. A clean glass slide was measured as a background reference. The thickness of different layers were measured using a Dektak 3 profilometer (Veeco Instruments Inc.). AFM images were captured with a Bruker Dimension Icon atomic force microscope, in peak force tapping mode. Images were then analysed using Gwyddion.

**2.2.3 Kelvin probe & electroabsorption spectroscopy measurements.** We used a Besocke DeltaPhi Kelvin probe for measuring the contact potential difference of samples. Measurements were performed in darkness. The results were corrected by using as reference a freshly-cleaved highly oriented pyrolytic graphite (HOPG) sample that has a known work function of 4.475 eV.

In electroabsorption spectroscopy we probe the manifestation of non-linear optical effects that cause a variation in the absorption spectrum of the system of interest due to the application of a modulating electric field. More specifically we measure the normalised variation of light transmitted through a sample upon application of a periodic electric field. The schematic of the home-built apparatus used to perform the measurement is shown in Fig. S2 (ESI<sup>†</sup>). More details regarding the apparatus and method by which the built-in voltage is extracted can be found in previous work.<sup>35,36</sup> In brief, the response of our system can be modelled using the framework of Stark effect theory.<sup>37</sup> This leads to the equation  $\frac{\Delta T}{T} = -2G(h\nu)(V_{DC} - V_{BI})V_{AC}$ , where  $\frac{\Delta T}{T}$  is the electroabsorption signal,  $G(h\nu)$  describes the spectral dependence,  $V_{DC}$  is the applied DC voltage,  $V_{BI}$  is the built-in voltage and  $V_{AC}$  is the applied AC voltage. As evident from the equation, application of a DC voltage equal to the built-in voltage will cause the signal to vanish. Hence the built-in voltage of a device can be extracted at the point where the applied DC voltage nulls the signal. The above analysis assumes that there are no interfering spectral contributions (e.g. from permanent dipole moments possibly associated to polar molecules). To confirm this, we plot electroabsorption spectra with different applied DC and AC voltages and show that the isosbestic points always intersect at the point where the electroabsorption signal is nulled, hence there are no interfering contributions (that would cause the isosbestic point to shift) confirming the validity of using the stated method.<sup>38</sup>

## 3 Results and discussion

### 3.1 ZnO/MgO based inverted organic photovoltaics

The current density–voltage characteristics at 1 sun for OPVs based on a single ZnO ETL *vs.* the bilayer ZnO/MgO ETL (where

MgO was deposited at 5000 rpm or 3000 rpm) are shown in Fig. 1c. The corresponding average key photovoltaic performance indicators are set out in Table 1. The active materials used in the blend are PTB7-Th and PC<sub>70</sub>BM. The application of the ZnO/MgO bilayer rather than the single ZnO layer (when MgO is kept sufficiently thin  $\sim 10$  nm) successfully enhances the performance, boosting the PCE by  $\sim 10\%$ . This is achieved mainly through an increase in  $J_{sc}$  and in the FF. The increase in  $J_{sc}$  has also been verified by the calculation of the photocurrent from EQE spectra (Fig. S3 and Table S1, ESI<sup>†</sup>) which is in agreement with the extracted data from the current density–voltage investigations. It is important to note that the efficient operation of OPVs employing the MgO interlayer requires the layer to be kept ultrathin. For the case of the thicker MgO devices (spin-coated at 3000 rpm with resulting thickness of  $\sim 150$  nm) a poor performance is obtained with an efficiency of  $0.03 \pm 0.02\%$ . This is a result of a very low  $J_{sc}$  of  $0.2 \pm 0.1$  mA cm<sup>-2</sup> and FF of  $0.26 \pm 0.02$ . The origin of the aforementioned changes in performance is investigated and discussed in detail in Section 3.2.

To demonstrate that the application of an MgO bilayer ETL can be extended to more types of OPVs, we have applied this strategy to other systems as well and assessed its effectiveness. The representative current density–voltage characteristic curves and the corresponding average key photovoltaic performance indicators for all the modifications can be found in Fig. S4 and Table S2 (ESI<sup>†</sup>). Where not otherwise specified the MgO precursor was spin-coated at 5000 rpm. Firstly, we substituted the Au top contact with Ag (that can serve as a cheaper alternative) and also tested devices without the MoO<sub>3</sub> HTL. Although the PCE of these devices is lower than the devices presented in Fig. 1, in all cases, the use of the bilayer MgO ETL instead of the single ETL boosted the performance through an increase in the  $J_{sc}$  and FF. We also tested OPVs with an SnO<sub>2</sub> ETL, however these devices yielded an “s-shaped” current density–voltage characteristic curve. Such an “s-shaped” curve for SnO<sub>2</sub> only ETLs in OPV devices have been previously reported in the literature, *e.g.* by Tran *et al.*<sup>41</sup> The physical mechanism responsible for this behaviour has been attributed to accumulation of charge carriers within the device.<sup>42</sup> Tran *et al.* mitigated the occurrence of “s-shaped” characteristics by incorporating a bilayer SnO<sub>2</sub>/CsCO<sub>3</sub> ETL in the device structure. Similarly, our SnO<sub>2</sub>/MgO bilayer removes some of the “s-shape” behavior. Finally, devices with a blend containing the non-fullerene acceptor ITIC-2F rather than PC<sub>70</sub>BM as the acceptor have also been tested. The substitution of the single ZnO ETL to the ZnO/MgO ETL for these devices led to an efficiency boost of  $\sim 15\%$  in relative terms, further demonstrating the wider applicability of MgO based bilayer ETLs in OPVs.

### 3.2 The effects of MgO as a top component in bilayer electron transport layers

While the effectiveness and reproducibility of the ZnO/MgO ETL for OPVs is demonstrated in Section 3.1, it is essential to understand the effects of introducing the ultrathin MgO



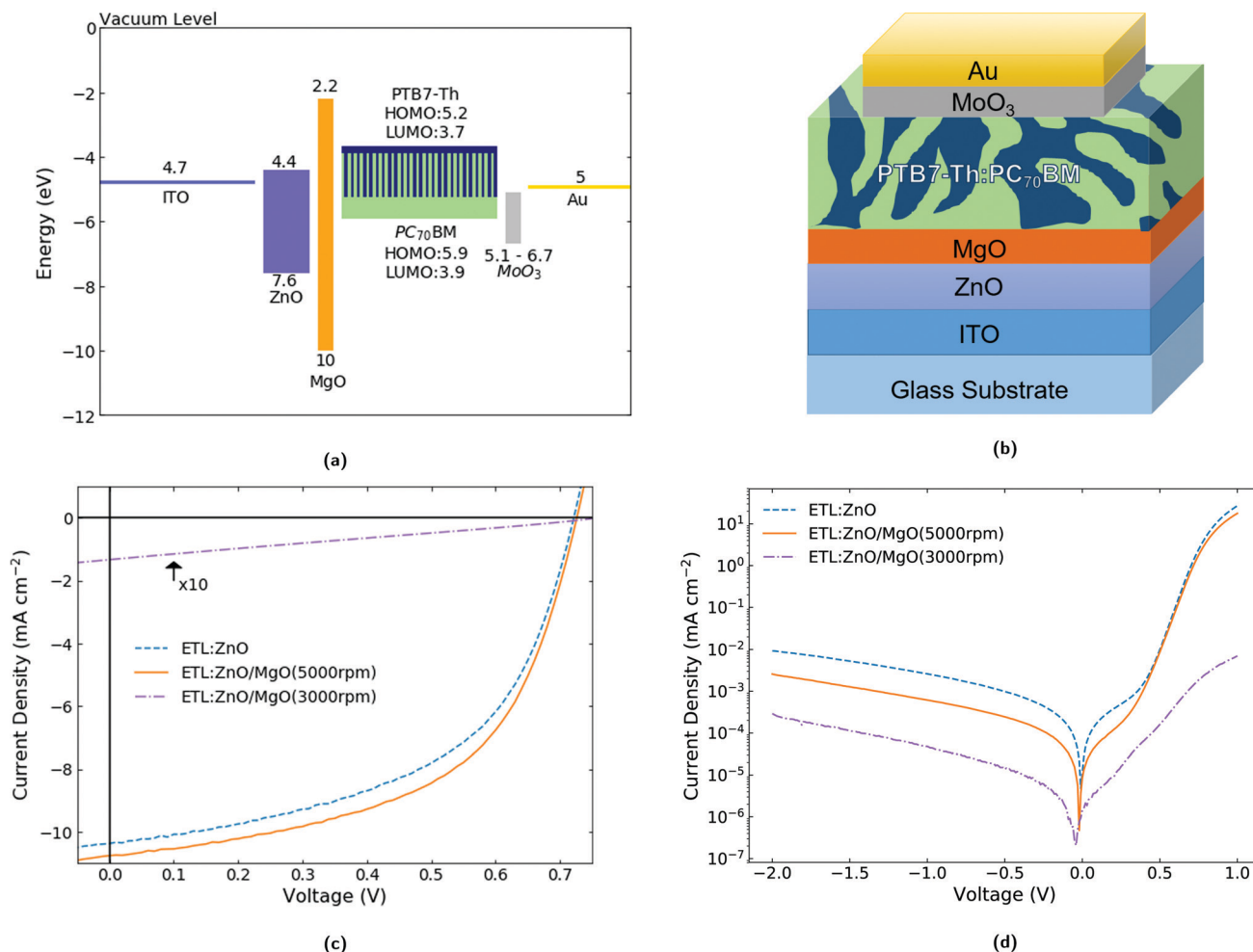


Fig. 1 (a) Approximate energy levels for the different components used in the OPV device (values have been obtained from the literature<sup>18,29,36,39,40</sup>). In the case of MoO<sub>3</sub> we report a relatively large range (please note the rectangle is not meant to indicate the energy gap but the spread of reported values of work function) since it is known that the work function depends strongly on the preparation conditions. We had also measured values  $\sim 5.1$  eV in our own laboratory. The thicknesses of the layers are approximately 30 nm (ZnO), 10/150 nm (MgO), 100 nm (active layer), 10 nm (MoO<sub>3</sub>) and 80 nm (Au). (b) Schematic of the multi-layered structure of the OPV device. (c) Representative current density-voltage curves under 1 sun. Here the current density for the device with the thicker MgO layer (150 nm) has been multiplied by a factor of 10 to aid legibility. The thickness of the MgO layer is  $\sim 10$  and 150 nm when the precursor is spin-coated at 5000 and 3000 rpm respectively. Note the very slight but clearly visible change in  $V_{oc}$  ( $\sim 5$  mV) for the selected devices. (d) Representative current density-voltage curves in the dark.

**Table 1** Variation in key photovoltaic parameters of OPVs based on a single ZnO ETL vs. the bilayer ZnO/MgO ETL. Averages from 7 distinct devices with multiple measurements for each device

Sample	PCE (%)	$J_{sc}$ (mA cm <sup>-2</sup> )	$V_{oc}$ (V)	FF
ITO/ZnO/PTB7-Th:PC <sub>70</sub> BM/MoO <sub>3</sub> /Au	3.98 $\pm$ 0.16	10.6 $\pm$ 0.5	0.72 $\pm$ 0.01	0.53 $\pm$ 0.03
ITO/ZnO/MgO(5000 rpm)/PTB7-Th:PC <sub>70</sub> BM/MoO <sub>3</sub> /Au	4.31 $\pm$ 0.14	10.9 $\pm$ 0.2	0.72 $\pm$ 0.01	0.55 $\pm$ 0.02
ITO/ZnO/MgO(3000 rpm)/PTB7-Th:PC <sub>70</sub> BM/MoO <sub>3</sub> /Au	0.03 $\pm$ 0.02	0.2 $\pm$ 0.1	0.73 $\pm$ 0.01	0.26 $\pm$ 0.02

modifying film in the OPV devices. In general, an increase in performance similar to the one we witnessed in the previous section is likely to be associated with one (or more) of the following mechanisms:<sup>18</sup>

(1) An improved rate of photon capture which depends strongly on the transmittance of the semi-transparent cell electrode.

(2) A favorable change in the active layer blend morphology leading to higher exciton dissociation.

(3) Reduced leakage current leading to a higher shunt resistance.

(4) A change in the interfacial energetics of the interface between the ETL and blend by a variation of the ETL's work function.

In the rest of this section we present evidence to help establish the extent to which the above mechanisms occur due to the presence of MgO and identify the origin of the success of MgO as an interlayer for OPVs.



**3.2.1 Transmittance.** To assess whether the ultrathin MgO interlayer leads to an improved rate of photon capture, we performed absorbance and transmittance measurements on thin films as displayed in Fig. 2. The addition of MgO on top of ZnO, seems to have a negligible effect in altering the transmittance. Moreover, the absorbance spectra of films also incorporating the PTB7-Th:PC<sub>70</sub>BM blend are almost identical for ITO/ZnO and ITO/ZnO/MgO(5000 rpm) substrates. It is therefore improbable that an improved rate of photon capture is achieved *via* the addition of MgO and hence another mechanism is most likely responsible for the favorable performance enhancements associated with the presence of MgO.

**3.2.2 Morphology.** AFM measurements were carried out to investigate variations in the surface morphology and rms roughness of the PTB7-Th:PC<sub>70</sub>BM blend when deposited on ITO/ZnO and ITO/ZnO/MgO(5000 rpm) substrates. Furthermore, samples of ITO/ZnO and ITO/ZnO/MgO(5000 rpm) without the blend layer were characterised. The 1.6  $\mu\text{m} \times 1.6 \mu\text{m}$  AFM images of the above investigations are presented in Fig. 3. To allow for comparison, we generated images of the samples to have the same height scale (10 nm for samples with blend and 35 nm for samples without blend). The surface morphology of

the samples with the blend is almost indistinguishable with an identical surface roughness of  $1.0 \pm 0.1 \text{ nm}$ . We have also tested samples with the structure ITO/PTB7-Th:PC<sub>70</sub>BM *vs.* ITO/MgO(5000 rpm)/PTB7-Th:PC<sub>70</sub>BM (see Fig. S5 and Table S3, ESI†) and there was no change in the blend morphology from the presence of MgO for these samples either. Therefore, regarding the mechanism by which MgO facilitates performance enhancement, it is unlikely that it is associated with a favorable change in the blend morphology since any changes in the bulk of the blend would have also very likely been manifested in the uppermost surface characterised by the AFM investigation. On the other hand, for the bare ITO/ZnO *vs.* ITO/ZnO/MgO(5000 rpm) samples, the AFM image of the sample that incorporates an MgO uppermost layer, appears much darker. This corresponds to peaks of shorter height correlated with a more uniform upper surface with the rms roughness decreasing from  $4.5 \pm 0.2 \text{ nm}$  to  $3.2 \pm 0.4 \text{ nm}$ . A lower surface roughness is manifested when MgO is deposited on SnO<sub>2</sub> as well, as shown by Dagar *et al.*<sup>29</sup> Contradictory reports can be found in the literature regarding how the surface roughness of the ETL affects the PCE of OPVs. Some reports show enhanced photovoltaic performance upon an increase in rms roughness<sup>20,43</sup> while others support that an increase in performance is a result of a lower surface roughness.<sup>18,19,25,27,41</sup> Both cases are equally valid but need a further distinction. If the increased roughness is a result of forming specific nanopatterns that aim to change the morphology of the photovoltaic blend, then this may be accompanied by an increase in performance. In the case where a change in morphology is not targeted, as is the case of the system presented herein, the lower roughness is indicative of a more homogeneous top surface of the ETL, with fewer pinholes. This is beneficial as it decreases the number of defective interfaces where recombination can happen and can lead to a reduction in pathways for current leakage that can lead to an increase in performance.

**3.2.3 Leakage currents.** Evidence of the reduced current leakage in the system consisting of the MgO interlayer is presented in Fig. 1d where the current density–voltage curves for the OPV devices in the dark are shown. Addition of MgO reduces the leakage current which is indicative of an increased effective shunt resistance for the bilayer device.<sup>44,45</sup> The average current density at  $-1 \text{ V}$  of the ITO/ZnO/PTB7-Th:PC<sub>70</sub>BM/MoO<sub>3</sub>/Au devices in dark conditions is  $-2.9 \times 10^{-3} \text{ mA cm}^{-2}$  and the shunt resistance is  $5.82 \times 10^5 \Omega \text{ cm}^2$ . The methodology for extracting the shunt resistance is detailed in the ESI.† In the case of the ITO/ZnO/MgO(5000 rpm)/PTB7-Th:PC<sub>70</sub>BM/MoO<sub>3</sub>/Au devices the presence of the MgO layer leads to halving of the leakage current at  $-1 \text{ V}$  (down to  $-1.7 \times 10^{-3} \text{ mA cm}^{-2}$ ) and to an increase of the shunt resistance to almost double the value of the device without MgO, *i.e.* up to  $8.35 \times 10^5 \Omega \text{ cm}^2$ . The increased shunt resistance prevents power losses that can occur *via* alternative current paths and is conducive to the observed increase in FF for the devices measured under illumination.<sup>46</sup> The observed increase in  $J_{\text{sc}}$  under illumination is also partly attributed to the increased shunt resistance and the slight variation of the overall electrode work function (*vide infra*), and therefore built-in voltage. It is likely that a decreased series

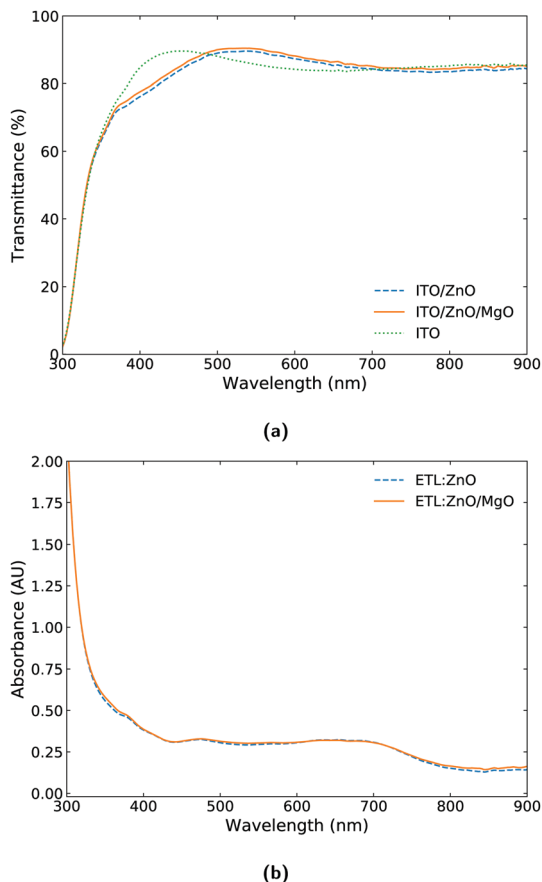


**Fig. 2** (a) Transmittance of ITO, ITO/ZnO, ITO/ZnO/MgO(5000 rpm) films. (b) Absorbance spectra of thin films comparing the ITO/ZnO/PTB7-Th:PC<sub>70</sub>BM with the ITO/ZnO/MgO(5000 rpm)/PTB7-Th:PC<sub>70</sub>BM structures. The addition of MgO seems to have a negligible effect.



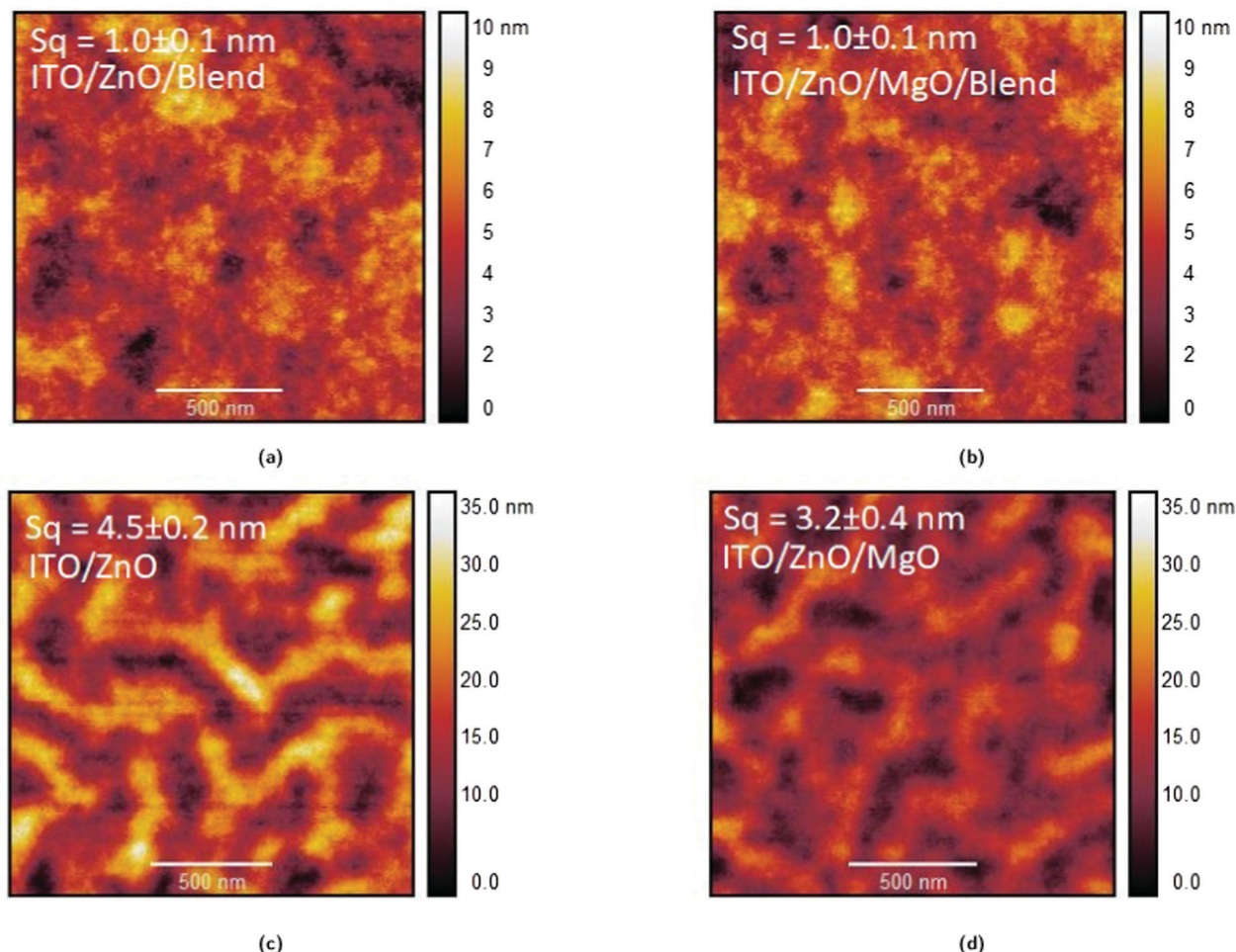


Fig. 3 Tapping mode AFM images of the topography of (a) ITO/ZnO/PTB7-Th:PC<sub>70</sub>BM, (b) ITO/ZnO/MgO(5000 rpm)/PTB7-Th:PC<sub>70</sub>BM where surface morphology is almost indistinguishable and (c) ITO/ZnO, (d) ITO/ZnO/MgO(5000 rpm) where a variation in root mean square (rms) roughness is observed.

resistance is also the result of the ultrathin MgO addition, that could also lead to an increase in  $J_{sc}$ . In line with other literature we also refrain from extracting the series resistance due to the complications detailed in the ESI,<sup>†</sup> that make it difficult to extract reliable conclusions. Current density–voltage characteristics in the dark for devices consisting of ITIC-2F rather than PC<sub>70</sub>BM as the acceptor are presented in Fig. S6 and Table S4 (ESI<sup>†</sup>). Similarly, a decreased current leakage is observed for devices based on the bilayer ETL. This is accompanied by an increase in shunt resistance. For the case of the devices where a thicker MgO layer is employed (spin-coated at 3000 rpm, corresponding to  $\sim 150$  nm thickness), even though an even lower leakage current at  $-1$  V of  $-8.2 \times 10^{-5}$  mA cm<sup>-2</sup> and a higher shunt resistance of  $1.66 \times 10^6$   $\Omega$  cm<sup>2</sup> is achieved, the thick insulating layer results in a significant increase in the series resistance leading to a decreased  $J_{sc}$  and to the FF approaching a value of 0.25 (see Fig. S8, ESI<sup>†</sup>) and hence the very low efficiency of  $0.03 \pm 0.02\%$ . However, when the MgO interlayer is spin-coated at the higher speed of 5000 rpm this leads to a much thinner ( $\sim 10$  nm) interlayer that is also non-uniform. Lack of uniformity of the layer is evidenced by the

reduced surface roughness in the AFM investigation (from  $4.5 \pm 0.2$  nm to  $3.2 \pm 0.4$  nm) upon addition of MgO. It is likely that the MgO insulating interlayer is much thinner than 10 nm (therefore enabling efficient charge transport) in certain areas, and maintain a higher thickness (and insulating nature) in other areas. The question arises as to whether the relatively limited extent of the electrode's area that is effective for charge extraction might reduce the overall device performance. Interestingly, and as shown by Dabera *et al.*,<sup>47</sup> it is possible for  $\sim 99\%$  of the surface of an ETL to be electrically insulating without eroding the efficiency of charge carrier extraction given that sufficient pathways for conduction remain. Our ultrathin and non-uniform MgO interlayer appears to provide a general suppression of the leakage current (*e.g.* due to interfacial recombination), and so a higher shunt resistance, while simultaneously preserving sufficient “charge transparency”, presumably through the thinner MgO regions.

**3.2.4 Work function and energy level alignment.** Another very important parameter affecting the properties of the interface between an ETL and the active material is the



matching of the work function of the ETL with the lowest unoccupied molecular orbital level (LUMO) of the acceptor material.<sup>11</sup> We have investigated whether the application of ultrathin MgO on metal oxides alters the work function of the system by use of a Kelvin probe. The change in work function ( $\Delta W$ ) upon addition of the MgO layer on top of three types of metal oxides is shown in Table 2. In all three cases, the work function decreases with the addition of MgO. In the case of ITO we observe a substantial decrease of 0.5 eV, whereas for the ITO/ZnO substrate, the decrease of the work function upon addition of MgO is of the order of 0.1 eV. Such changes and the possible causes for the difference in  $\Delta W$  between different metal oxides is investigated in detail in Section 3.3. The LUMO level of PC<sub>70</sub>BM is reported to be  $-3.9$  eV<sup>39</sup> whereas the ITO/ZnO work function was measured by Kelvin probe to be 4.76 eV. By applying the MgO layer and reducing the work function to 4.66 eV, we reduce the relevant energy level mismatch and therefore the losses connected with charge extraction. Such a modification to the work function may be manifested as a change in the built-in voltage of the completed device. To measure changes in the built-in voltage we employ electroabsorption spectroscopy.<sup>35</sup> As we are interested in probing the change caused by the addition of MgO in the device structure, we characterise devices free of an HTL that provide a clearer demonstration of changes only occurring at the ETL/blend interface. Fig. 4 shows the variation of the electroabsorption signal with DC voltage for the single ZnO ETL device and the device incorporating the bilayer ZnO/

MgO(5000 rpm) ETL. The built-in voltage can be extracted at the point of intersection of the electroabsorption signal variation with the  $\Delta T/T = 0$  line. The presence of MgO leads to a shift in the built-in voltage ( $\Delta V_{BI}$ ) by  $0.05 \pm 0.03$  V as calculated from the difference in the built-in voltages extracted from the plot. We have also extracted the shift in built-in voltage for the devices that employ ITIC-2F rather than PC<sub>70</sub>BM as the acceptor (see Fig. S9, ESI†) to be  $0.10 \pm 0.03$  V. The values are in agreement with the expected measurement of work function shift from the kelvin probe investigations. An increase in built-in potential (and thus a higher internal field) can lead to reduced recombination losses and elimination of the buildup of space charge and can partly explain the higher  $J_{sc}$  and FF achieved<sup>48</sup> for the devices described in Section 3.1. Often, a change in the built-in voltage results in a change in the  $V_{oc}$  of devices as well. We do not exclude this possibility, since a visible change in  $V_{oc}$  (5 mV) is shown in Fig. 1c, however, scatter from device to device washes out the slight difference in  $V_{oc}$  in the average. For devices with thicker MgO layers a bigger shift in  $V_{oc}$  of 0.1 V is obtained. This is likely the result of a more complete coverage of the MgO layer. The work function shifts caused by the application of MgO for the ITO and ITO/SnO<sub>2</sub> devices were also cross-checked using electroabsorption spectroscopy (see Fig. S9, ESI†). For these investigations we used F8BT as the active material. The measured changes in built-in voltage for these materials are found in Table 2. The shift in work function is consistent with the change in built-in voltage in both cases.

**Table 2** The difference in work function and built-in voltage between samples with and without MgO(5000 rpm) for the three tested substrates

Sample	Active layer	$\Delta W$ (eV)	$\Delta V_{BI}$ (V)
ITO/(MgO)	F8BT	$-0.50 \pm 0.05$	$0.46 \pm 0.03$
ITO/ZnO/(MgO)	Blend	$-0.11 \pm 0.05$	$0.05 \pm 0.03$
ITO/SnO <sub>2</sub> /(MgO)	F8BT	$-0.20 \pm 0.05$	$0.19 \pm 0.03$

### 3.3 Origin of the work function modification by the addition of MgO

The application of MgO and work function modification on different metals and semiconductors has been extensively studied in the literature as a promising solution for catalysis.<sup>49</sup> Three main mechanisms that have been identified to dictate work function modifications in general are the

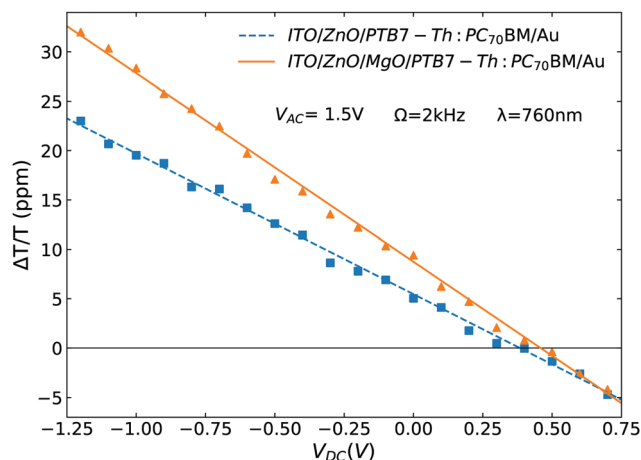


**Fig. 4** Electroabsorption signal vs. DC voltage plots used to extract the built-in voltage in the single ETL and bilayer ETL OPV devices. The parameters used for the experiments are displayed in the Figure. The MgO layer thickness is  $\sim 10$  nm for the relevant device.

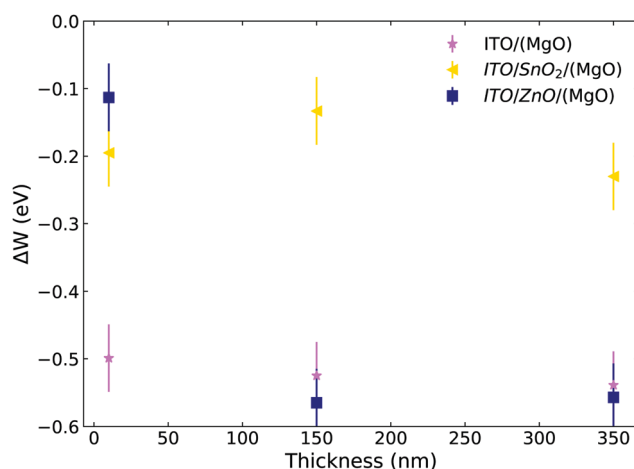


**Fig. 5** Kelvin probe measurements showing the change in the work function of different substrates upon addition of the MgO layer with varying thickness.



electrostatic compressive effect, charge transfer and surface relaxation. For the case of MgO, the electrostatic compressive effect can give a significant contribution.<sup>34</sup> This effect enables the MgO layer to form a surface dipole on the metal or semiconductor surface even in the absence of charge transfer. The different levels of the contribution of these mechanisms can give considerable differences in the final change in work function, hence the change in work function can be rather different for different substrate materials. This explains why such different values of work function shift ( $\Delta W$ ) are observed upon MgO application for the different substrates used in our investigations (as shown in Table 2). In Fig. 5 we present further Kelvin probe measurements of the dependence of work function shift ( $\Delta W$ ) on the thickness of MgO deposited on top of the substrate. The thicknesses are approximately 10, 150 and 350 nm as measured by profilometry corresponding to 5000, 3000 and 1000 rpm spin coating deposition speeds. The reduction of work function seems to be thickness independent for ITO and ITO/SnO<sub>2</sub>, whilst for ITO/ZnO, it seems to be thickness dependent only at very small thicknesses (which may be a result of partial coverage). This overall thickness independence points towards an interfacial mechanism being responsible for the decrease in work function and hence our findings further support and are in line with the established findings in the literature.

## 4 Conclusions

In this work, we have investigated the application of low cost, non-toxic ultrathin ( $\sim 10$  nm) MgO as a potential modifying interlayer to serve as the top component of bilayer ETLs applied to OPVs. The use of the ZnO/MgO bilayer rather than single ZnO as ETL, led to a  $\sim 10\%$  and  $\sim 15\%$  increase in efficiency in relative terms for devices consisting of a blend with a fullerene acceptor and a non-fullerene acceptor respectively. The increase in PCE was a result of an enhanced  $J_{sc}$  and FF, which we can trace down to a reduction in the leakage current and an increase in the shunt resistance of devices. The presence of MgO leads to a number of favourable characteristics. Without significantly affecting the photon capture rate and blend morphology, the MgO interlayer offers an improved contact as demonstrated by the reduction of the surface roughness of the ETL and the lower work function. This leads to a better energy level matching with the LUMO of the photovoltaic blend acceptor that results in enhanced charge extraction. The lower work function is shown to originate from an interfacial interaction between the MgO and the metal oxide that is consistent with the so-called electrostatic compressive effect. Through our investigations, we show that high transparency and a high ionisation potential can serve as useful design rules for future ETLs but more importantly our study serves as proof that inspiration for future ETLs for OPVs can be drawn by novelties in other solution-processed systems and that transfer of developments from one field to another can be a viable route to synergistically push the performance boundaries of these promising technologies to even higher levels.

## Conflicts of interest

There are no conflicts to declare.

## Acknowledgements

Special thanks to Natalie Stingelin, Alessandro Minotto and Andrea Zampetti for useful discussions. We acknowledge use of the London Centre for Nanotechnology Atomic Force Microscope Facility. It was supported by the EPSRC and SFI Centre for Doctoral Training in Advanced Characterisation of Materials (grant number EP/L015277/1). TMB received support from MIUR through the PRIN2017 BOOSTER project (no. 2017YXX8AZ). FC thanks EPSRC for financial support *via* grant EPSRC: EP/P007767/1.

## Notes and references

- 1 M. Graetzel, R. A. J. Janssen, D. B. Mitzi and E. H. Sargent, *Nature*, 2012, **488**, 304–312.
- 2 I. Ierides, A. Zampetti and F. Cacialli, *Curr. Opin. Green Sustainable Chem.*, 2019, **17**, 15–20.
- 3 M. Y. M. Liu and E. H. Sargent, *Nat. Energy*, 2016, **1**, 16016.
- 4 K. A. Mazzio and C. K. Luscombe, *Chem. Soc. Rev.*, 2015, **44**, 78–90.
- 5 C. Yan, S. Barlow, Z. Wang, H. Yan, A. K.-Y. Jen, S. R. Marder and X. Zhan, *Nat. Rev. Mater.*, 2018, **3**, 18003.
- 6 S. D. Collins, N. A. Ran, M. C. Heiber and T.-Q. Nguyen, *Adv. Energy Mater.*, 2017, **7**, 1602242.
- 7 Q. Lin, A. Armin, P. L. Burn and P. Meredith, *Acc. Chem. Res.*, 2016, **49**, 545–553.
- 8 P. Papagiorgis, A. Manoli, S. Michael, C. Bernasconi, M. I. Bodnarchuk, M. V. Kovalenko, A. Othonos and G. Itskos, *ACS Nano*, 2019, **13**, 5799–5809.
- 9 J. Dagar, S. Castro-Hermosa, G. Lucarelli, A. Zampetti, F. Cacialli and T. M. Brown, *IEEE J. Photovolt.*, 2019, **9**, 1309–1315.
- 10 R. J. E. Westbrook, D. I. Sanchez-Molina, D. J. Manuel Marin-Beloqui, D. H. Bronstein and D. S. A. Haque, *J. Phys. Chem. C*, 2018, **122**, 1326–1332.
- 11 J.-H. Lee, S. Y. Jeong, G. Kim, B. Park, J. Kim, S. Kee, B. Kim and K. Lee, *Adv. Funct. Mater.*, 2018, **28**, 1705079.
- 12 Z. Yin, J. Wei and Q. Zheng, *Adv. Sci.*, 2016, **3**, 1500362.
- 13 Z. He, C. Zhong, S. Su, M. Xu, H. Wu and Y. Cao, *Nat. Photonics*, 2012, **6**, 591–595.
- 14 H.-L. Yip and A. K.-Y. Jen, *Energy Environ. Sci.*, 2012, **5**, 5994–6011.
- 15 P. Li, Z. Jiang, H. Huang, S. Tian, X. Hu, W. Li, X. Bao and Y. Wang, *Mater. Sci. Semicond. Process.*, 2020, **116**, 105150.
- 16 Y. Lin, Y. Firdaus, M. I. Nugraha, F. Liu, S. Karuthedath, A.-H. Emwas, W. Zhang, A. Seikhan, M. Neophytou, H. Faber, E. Yengel, I. McCulloch, L. Tsetseris, F. Laquai and T. D. Anthopoulos, *Adv. Sci.*, 2020, **7**, 1903419.
- 17 X. Du, Y. Yuan, L. Zhou, H. Lin, C. Zheng, J. Luo, Z. Chen, S. Tao and L.-S. Liao, *Adv. Funct. Mater.*, 2020, **30**, 1909837.



- 18 C. Wang, D. Luo, Y. Gao, G. Wang, C. Wang, P. Ma, H. Li, S. Wen, W. Dong and S. Ruan, *J. Phys. Chem. C*, 2019, **123**, 16546–16555.
- 19 J. Xie, X. Wang, S. Wang, Z. Ling, H. Lian, N. Liu, Y. Liao, X. Yang, W. Qu, Y. Peng, W. Lan and B. Wei, *Org. Electron.*, 2019, **75**, 105381.
- 20 M. Abd-Ellah, J. Cann, S. V. Dayneko, A. Laventure, E. Cieplechowiec and G. C. Welch, *ACS Appl. Electron. Mater.*, 2019, **1**, 1590–1596.
- 21 X. Zhang, Y. Sun, M. Wang, H. Cui, W. Xie, L. Shen and W. Guo, *Sol. Energy*, 2019, **181**, 9–16.
- 22 Y. Tang, Y. Pang, X. Li, B. Zong, B. Kang, S. R. P. Silva and G. Lu, *J. Colloid Interface Sci.*, 2020, **562**, 142–148.
- 23 X. Cai, T. Yuan, X. Liu and G. Tu, *ACS Appl. Mater. Interfaces*, 2017, **9**, 36082–36089.
- 24 A. Soultati, A. Verykios, S. Panagiotakis, K.-K. Armadorou, M. I. Haider, A. Kaltzoglou, C. Drivas, A. Fakharruddin, X. Bao, C. Yang, A. R. B. M. Yusoff, E. K. Evangelou, I. Petsalakis, S. Kennou, P. Falaras, K. Yannakopoulou, G. Pistolis, P. Argitis and M. Vasilopoulou, *ACS Appl. Mater. Interfaces*, 2020, **12**, 21961–21973.
- 25 Y.-Y. Yu, C. Tseng, W.-C. Chien and C.-P. Chen, *Org. Electron.*, 2019, **69**, 20–25.
- 26 J. Dagar, G. Scavia, M. Scarselli, S. Destri, M. De Crescenzi and T. M. Brown, *Nanoscale*, 2017, **9**, 19031–19038.
- 27 Q. Rong, Q. Zhang, M. Cui, L. Nian, D. Zheng, X. Gao, L. Shui, G. Zhou and N. Li, *Org. Electron.*, 2020, **81**, 105669.
- 28 Q. Liu, Y. Jiang, K. Jin, J. Qin, J. Xu, W. Li, J. Xiong, J. Liu, Z. Xiao, K. Sun, S. Yang, X. Zhang and L. Ding, *Sci. Bull.*, 2020, **65**, 272–275.
- 29 J. Dagar, S. Castro-Hermosa, G. Lucarelli, F. Cacialli and T. M. Brown, *Nano Energy*, 2018, **49**, 290–299.
- 30 G. S. Han, H. S. Chung, B. J. Kim, D. H. Kim, J. W. Lee, B. S. Swain, K. Mahmood, J. S. Yoo, N.-G. Park, J. H. Lee and H. S. Jung, *J. Mater. Chem. A*, 2015, **3**, 9160–9164.
- 31 E. N. Jayaweera, G. R. Kumara, C. Kumarage, S. K. Ranasinghe, R. M. G. Rajapakse, H. M. N. Bandara, O. A. Ileperuma and B. S. Dassanayake, *J. Photochem. Photobiol. A*, 2018, **364**, 109–115.
- 32 P. Docampo, P. Tiwana, N. Sakai, H. Miura, L. Herz, T. Murakami and H. J. Snaith, *J. Phys. Chem. C*, 2012, **116**, 22840–22846.
- 33 S. Huang, B. Kang, L. Duan and D. Zhang, *J. Colloid Interface Sci.*, 2021, **583**, 178–187.
- 34 S. Prada, U. Martinez and G. Pacchioni, *Phys. Rev. B*, 2008, **78**, 235423.
- 35 T. M. Brown, J. S. Kim, R. H. Friend, F. Cacialli, R. Daik and W. J. Feast, *Appl. Phys. Lett.*, 1999, **75**, 1679–1681.
- 36 T. M. Brown, G. M. Lazzerini, L. J. Parrott, V. Bodrozic, L. Bürgi and F. Cacialli, *Org. Electron.*, 2011, **12**, 623–633.
- 37 I. H. Campbell, T. W. Hagler, D. L. Smith and J. P. Ferraris, *Phys. Rev. Lett.*, 1996, **76**, 1900–1903.
- 38 E. Siebert-Henze, V. G. Lyssenko, J. Fischer, M. Tietze, R. Brueckner, M. Schwarze, K. Vandewal, D. Ray, M. Riede and K. Leo, *AIP Adv.*, 2014, **4**, 047134.
- 39 Ossila, PC70BM, <https://www.ossila.com/products/pc70bm>.
- 40 Ossila, PTB7-Th, PCE-10, <https://www.ossila.com/products/pce10>.
- 41 V.-H. Tran, S. H. Eom, S. C. Yoon, S.-K. Kim and S.-H. Lee, *Org. Electron.*, 2019, **68**, 85–95.
- 42 B. Qi and J. Wang, *Phys. Chem. Chem. Phys.*, 2013, **15**, 8972–8982.
- 43 F. Zhao, L. Deng, K. Wang, C. Han, Z. Liu, H. Yu, J. Li and B. Hu, *ACS Appl. Mater. Interfaces*, 2020, **12**, 5120–5127.
- 44 A. Savva, F. Petraki, P. Eleftheriou, L. Sygellou, M. Voigt, M. Giannouli, S. Kennou, J. Nelson, D. D. C. Bradley, C. J. Brabec and S. A. Choulis, *Adv. Energy Mater.*, 2013, **3**, 391–398.
- 45 M. Neukom, S. Züfle, S. Jenatsch and B. Ruhstaller, *Sci. Technol. Adv. Mater.*, 2018, **19**, 291–316.
- 46 M. Wang, Y. Sun, J. Guo, Z. Li, C. Liu and W. Guo, *Org. Electron.*, 2019, **74**, 258–264.
- 47 G. D. M. R. Dabera, J. Lee and R. A. Hatton, *Adv. Funct. Mater.*, 2019, **29**, 1904749.
- 48 S. Huang, N. Ali, Z. Huai, J. Ren, Y. Sun, X. Zhao, G. Fu, W. Kong and S. Yang, *Org. Electron.*, 2020, **78**, 105555.
- 49 T. Jaouen, G. Jézéquel, G. Delhaye, B. Lépine, P. Turban and P. Schieffer, *Appl. Phys. Lett.*, 2012, **100**, 022103.

